ADVANCED MATERIALS
www.advmat.de

A Self-Healing, Flowable, Yet Solid Electrolyte Suppresses Li-Metal Morphological Instabilities

Yubin He, Chunyang Wang, Ruoqian Lin, Enyuan Hu, Stephen E. Trask, Ju Li, and Huolin L. Xin**

Lithium metal (Li^0) solid-state batteries encounter implementation challenges due to dendrite formation, side reactions, and movement of the electrode–electrolyte interface in cycling. Notably, voids and cracks formed during battery fabrication/operation are hot spots for failure. Here, a self-healing, flowable yet solid electrolyte composed of mobile ceramic crystals embedded in a reconfigurable polymer network is reported. This electrolyte can auto-repair voids and cracks through a two-step self-healing process that occurs at a fast rate of 5.6 µm h^{-1}. A dynamical phase diagram is generated, showing the material can switch between liquid and solid forms in response to external strain rates. The flowability of the electrolyte allows it to accommodate the electrode volume change during Li^0 stripping. Simultaneously, the electrolyte maintains a solid form with high tensile strength (0.28 MPa), facilitating the regulation of mossy Li^0 deposition. The chemistries and kinetics are studied by operando synchrotron X-ray and in situ transmission electron microscopy (TEM). Solid-state NMR reveals a dual-phase ion conduction pathway and rapid Li^+ diffusion through the stable polymer-ceramic interphase. This designed electrolyte exhibits extended cycling life in Li^0–Li^0 cells, reaching 12 000 h at 0.2 mA cm^{-2} and 5000 h at 0.5 mA cm^{-2}. Furthermore, owing to its high critical current density of 9 mA cm^{-2}, the Li^0–$LiNi_{0.8}Mn_{0.1}Co_{0.1}O_2$ (NMC811) full cell demonstrates stable cycling at 5 mA cm^{-2} for 1100 cycles, retaining 88% of its capacity, even under near-zero stack pressure conditions.

1. Introduction

The use of lithium metal anode with a high specific capacity of 3860 mAh g^{-1} is promising for high-energy-density batteries.[1] Nonetheless, its practical implementation is hindered by interfacial challenges, such as nonuniform Li^0 deposition during charging and electrode–electrolyte delamination during discharge. Flowable liquid electrolytes facilitate consistent interface contact during electrode volume changes. However, their limited mechanical strength makes them more susceptible to dendrite formation (**Figure 1a**). In contrast, solid ceramic electrolytes (SCEs) exhibit a high modulus of 20–150 GPa,[2] which, according to the linear elasticity analyses by Monroe and Newman,[3] holds promise for mitigating uneven Li^0 growth. However, it became evident soon after that most SCEs exhibit poor cycling stability when paired with Li^0 anode.[4] This limitation arises from a complex interplay of chemical, electrochemical, and mechanical challenges, encompassing side reaction at electrode–electrolyte interface, high electron conductivity,[4] slow Li^+ diffusivity at grain boundaries.,[5] and electrode–electrolyte delamination.[6] Specifically, voids at the interface (Figure 1b) result in local current density concentration that accelerates dendrite growth.[7] and produce crack-tip stresses that drive crack propagation.[8] To address these issues, current solutions include introducing a soft buffer layer between the Li^0 anode and electrolyte,[9] utilizing alloy-based anodes.[10] to prevent dendrites, and applying high

Y. He, C. Wang, H. L. Xin
Department of Physics and Astronomy
University of California
Irvine, CA 92697, USA
E-mail: huolin.xin@uci.edu
R. Lin
Department of Mechanical Engineering
University of California
Riverside 92521, CA
E. Hu
Chemistry Division
Brookhaven National Laboratory
Upton NY 11973, USA
The ORCID identification number(s) for the author(s) of this article can be found under https://doi.org/10.1002/adma.202406315
S. E. Trask
Cell Analysis
Modeling
and Prototyping Facility
Argonne National Laboratory
Lemont, IL 60439, USA
J. Li
Department of Nuclear Science and Engineering
Massachusetts Institute of Technology
Cambridge, MA 02139, USA
E-mail: liju@mit.edu
J. Li
Department of Materials Science and Engineering
Massachusetts Institute of Technology
Cambridge, MA 02139, USA

DOI: 10.1002/adma.202406315

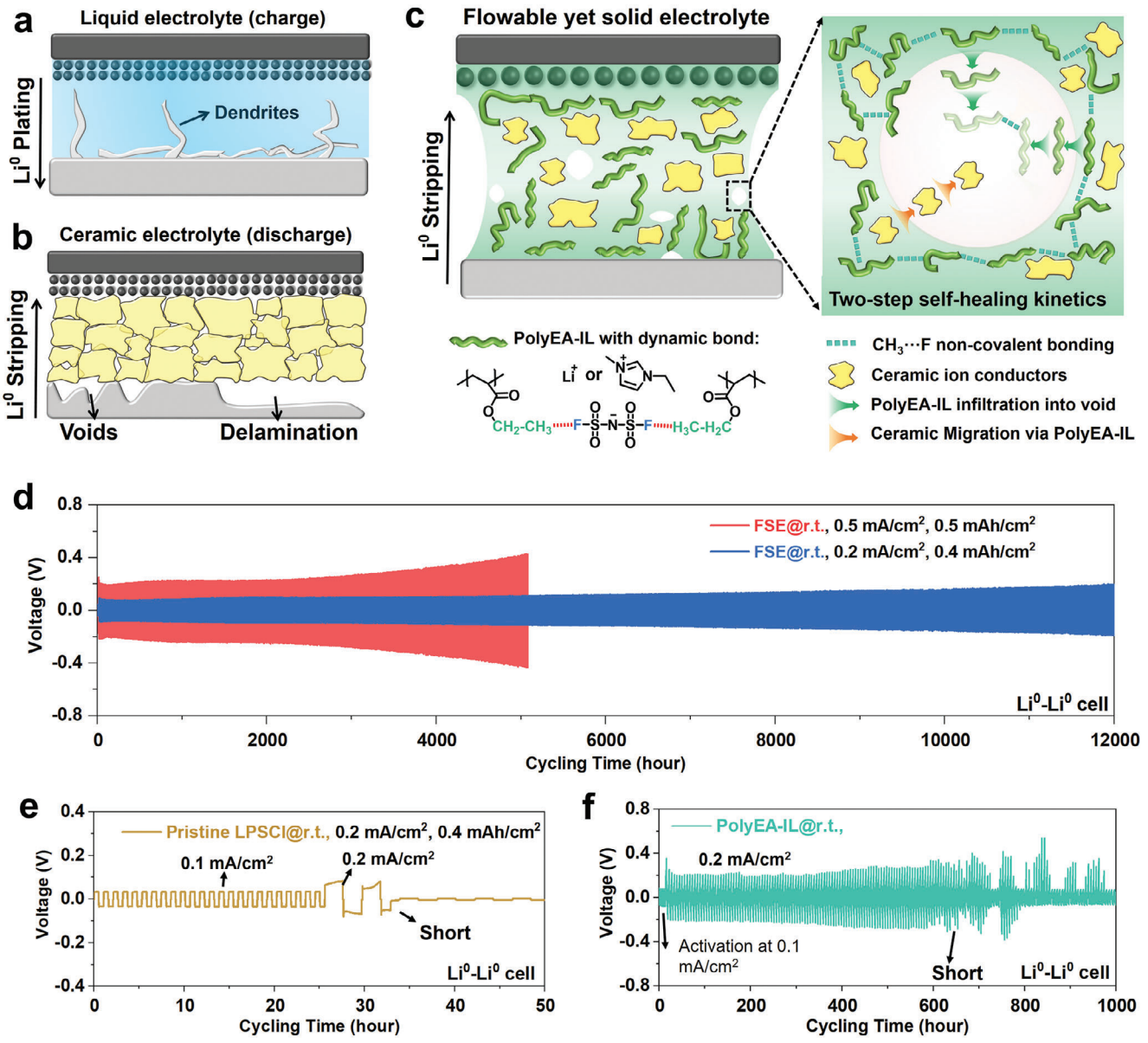

Figure 1. Designing concept and durability in Li^0–Li^0 cells. a,b) Schematic illustration showing the dendrite formation problem in conventional liquid electrolytes and the delamination issues in ceramic electrolytes. c) Schematic illustration showing the flowable yet solid electrolyte for suppressing the morphological instabilities of Li^0 anode. d–f) The durability of FSE d), pristine LPSCl e), and PolyEA-IL f) in Li^0–Li^0 cells at r.t. and under low stack pressure in coin cells. The cells were activated at 0.1 mA cm^{-2} for ≈20 h before cycling at 0.2 or 0.5 mA cm^{-2}. Enlarged voltage-time profiles are provided in Figures S2 and S3 (Supporting Information). The thickness of FSE, PolyEA-IL, and LPSCl electrolytes are 350, 350, and 800 µm, respectively.

stack pressure (40-100 MPa).[11] However, these approaches have limitations, such as uncontrolled dendrite growth in the buffer layer, reduced energy density, and impracticality for battery manufacturing. To establish a reliable solid-state Li^0 battery (SSLMB), three key challenges must be addressed: preventing void/crack formation, accommodating rapid Li^0 volume changes, and ensuring an adequate modulus to regulate Li^0 deposition. This presents conflicting demands on the mechanical properties of solid-state electrolytes (SSEs), requiring both softness to prevent delamination during discharge and solidity to inhibit dendrite penetration during charging.

Here, inspired by the concept of "Brownian motion in viscous flow," we have incorporated nonconstrained ceramics into a dynamic polymer network to integrate self-healing capability, flowability, and solid properties within a single electrolyte (Figure 1c). Our approach involves synthesizing a dynamic polymer (poly(ethyl acrylate)) with polymer-FSI^- and polymer-Li^+ noncovalent interactions (PolyEA-IL), followed by cold-milling with LPSCl crystals to produce the flowable yet solid electrolyte (FSE). The reversible noncovalent bonding and the high segmental mobility of PolyEA-IL imparted self-healing capabilities to the FSE and facilitated ceramic motion in the polymer matrix. As

depicted in Figure S1 (Supporting Information), the FSE is free-standing, flexible, and self-heals at room temperature. Using in situ, time-resolved TEM, we captured and quantified the motion of ceramic crystals through the dynamic polymer matrix, revealing a motion rate of 0.19 nm^{-1} s. This Brownian motion of ceramic crystals enables a two-step self-healing process, with sequential PolyEA-IL and LPSCl migration repairing voids up to 50 µm in size. Solid-state NMR reveals a dual-phase ion conduction pathway with rapid Li^+ diffusion through the stable polymer-ceramic interphase, yielding low grain boundary resistance (14 ohm cm^2) and high ionic conductivity (1.5 mS cm^{-1} at 30 °C). The liquid–solid transitioning properties of the dynamic polymer endows the FSE with elastic solid properties on shorter timescales and viscous flow on longer timescales. This flowability enables rapid adaptation to the moving Li^0 interface at a rate of 1.33 µm h^{-1}. Concurrently, the FSE remains an elastic solid with high tensile strength (0.28 MPa), effectively mitigating morphological instabilities in Li^0, as confirmed by cryogenic TEM (cryo-TEM). By addressing challenges associated with interfacial instability, mechanical degradation, and dendrite growth, the FSE exhibits durability of 12 000 h in Li^0–Li^0 symmetric cells (0.2 mA cm^{-2} at room temperature (r.t.), Figure 1d). In contrast, the LPSCl and PolyEA-IL baseline electrolytes experience short-circuiting within 40 and 700 h, respectively (Figure 1e,f).

2. Results and Discussion

2.1. Electrolyte Chemistry and Ion Conduction Pathway

Figure 2a illustrates the solvent-free, single-step UV polymerization chemistry used for PolyEA-IL synthesis. Magic angle spinning (MAS) solid-state ^{1}H NMR confirms nearly complete monomer conversion (≈100%, Figure S4a, Supporting Information), yielding a high molecular weight of 1.65×10^6 Da (Figure S4b, Supporting Information). Despite its high molecular weight, PolyEA-IL maintains a low glass transition temperature (T_g) of −55 °C (Figure S4c, Supporting Information) due to the plasticizing effect of the ionic liquid.[12] This enhanced segmental mobility promotes conformational changes and chain diffusion, facilitating the self-healing process.[13] Additionally, noncovalent interactions of Polymer•••Li^+ and polymer•••FSI^- offer reversible bonding for reconnecting cleaved polymer chains.[14] As evident in the ^{1}H solid-state NMR spectra (Figure 2b and Figure S45, Supporting Information), the $–CH_2–$ and $–CH_3$ signals undergo downfield shifts of 0.14 and 0.07 ppm, respectively, upon introducing the LiFSI. This de-shielding effect could be caused by interactions between Li^+ and the ester groups of the monomer[15] as no deuterium reagent that could interfere with NMR results was used.

To further demonstrate the polymer-anion interaction of –C–H•••F–SO_2–, we selected benzenesulfonyl fluoride (FSB) as a model compound (Figure S46, Supporting Information). FSB lacks a cation and contains only proton-accepting F–SO_2– groups, allowing us to investigate the effect of –C–H•••F–SO_2– hydrogen bonding without interference from cation-EA interactions. As shown in Figure S46 (Supporting Information), with increasing concentration of FSB in EA, the signals of $–CH_3$, $–CH_2–$, and CH_2 = CH– in EA gradually shifted upfield by 0.26, 0.22, and 0.23 ppm, respectively. Conversely, with increasing concentration of EA in FSB, the signals of FSB gradually shifted downfield by 0.4 ppm. This upfield shift (i.e., shielding effect) of EA signals aligns with previous literatures.[16] and can be explained by the high electron cloud density of the F–SO_2– group (δO^- and δF^-).[17] When forming the –C–H•••F–SO_2– interaction, the δO^- and δF^- dipoles share their lone pair with the H atom in EA, increasing the electron cloud density of EA molecules. This observation supports the presence of intermolecular –CH•••F–SO_2– bonding, consistent with prior studies utilizing FTIR or NMR characterizations.[18] Theoretical predictions also indicated a high binding energy of ≈0.5 eV.[19,20] notably exceeding the strength of water–water hydrogen bonding (0.25 eV).[21] Therefore, this polymer–anion interaction is widely applied in constructing functional polymers such as mechanically robust and stretchable ionogels.[18,22] In this study, besides enabling self-healing, this dynamic bonding undergoes continuous breaking-reforming processes,[23] facilitating the movement of embedded LPSCl particles. In contrast, conventional composite SSEs restrict ceramic motion due to crosslinked or crystallized polymer chains.[24] Additionally, this aprotic dynamic network eliminates the need for Li^0-reactive moieties (e.g., –OH and –NH–),[25] thereby enhancing its interfacial stability.

Using MAS solid-state NMR, we further elucidated the ion conduction pathway through a ^{7}Li to ^{6}Li isotope exchange approach. Cycling a ^{6}Li/FSE/^{6}Li symmetric cell resulted in the replacement of ^{7}Li ions within FSE by ^{6}Li ions, thus delineating the ion conduction pathway (Figure 2c). As depicted in Figure 2d, after cycling, the signal intensity for LPSCl at 1.44 ppm and PolyEA-IL at −1.17 ppm increased by 6.4-fold and 5.7-fold, respectively, due to the substitution of ^{7}Li by ^{6}Li. This confirms Li^+ diffusion through both PolyEA-IL and LPSCl, highlighting the efficacy of both the polymer and ceramic phases as ion conduction pathways. To further validate Li^+ diffusion across the polymer-ceramic interphase, we conducted 2D ^{6}Li–^{6}Li exchange spectroscopy (2D-EXSY) with a mixing time (T_{mix}) of 100 ms. Two prominent off-diagonal cross-peaks were observed (Figure 2e, as indicated by the black box), indicating Li^+ exchange between the local environments of the polymer and ceramic phases at the T_{mix} time scale.[26]

The stable interphase chemistry and rapid Li^+ diffusion results from the good chemical compatibility between PolyEA-IL and LPSCl. As evidenced in Figure 2f and Figure S5 (Supporting Information), the ^{6}Li NMR spectra of FSE and LPSCl exhibit no changes in line shape or chemical shift, confirming the absence of side reactions or interphase passivation layers. No shoulder peak around the PolyEA-IL resonance is observed, indicating a single Li^+ environment in the polymer phase without salt segregation or phase separation. Additionally, ^{1}H NMR spectra of PolyEA-IL and FSE in Figure 2g show no new signals or chemical shift alterations after hybridization with LPSCl, indicating no polymer chain degradation. Despite the stable interphase chemistry, solid-state NMR results also reveal noncovalent interactions between PolyEA-IL and LPSCl. The expanded ^{1}H NMR spectra (Figure S6, Supporting Information) show significant line broadening in FSE compared to PolyEA-IL, suggesting an anisotropic chemical environment within the polymer phase due to its interaction with LPSCl ceramics.[27] Additionally, the ^{6}Li signals of PolyEA-IL experienced a downfield shift from −1.42 to −1.19 ppm after hybridization (Figure 2f), indicating noncovalent

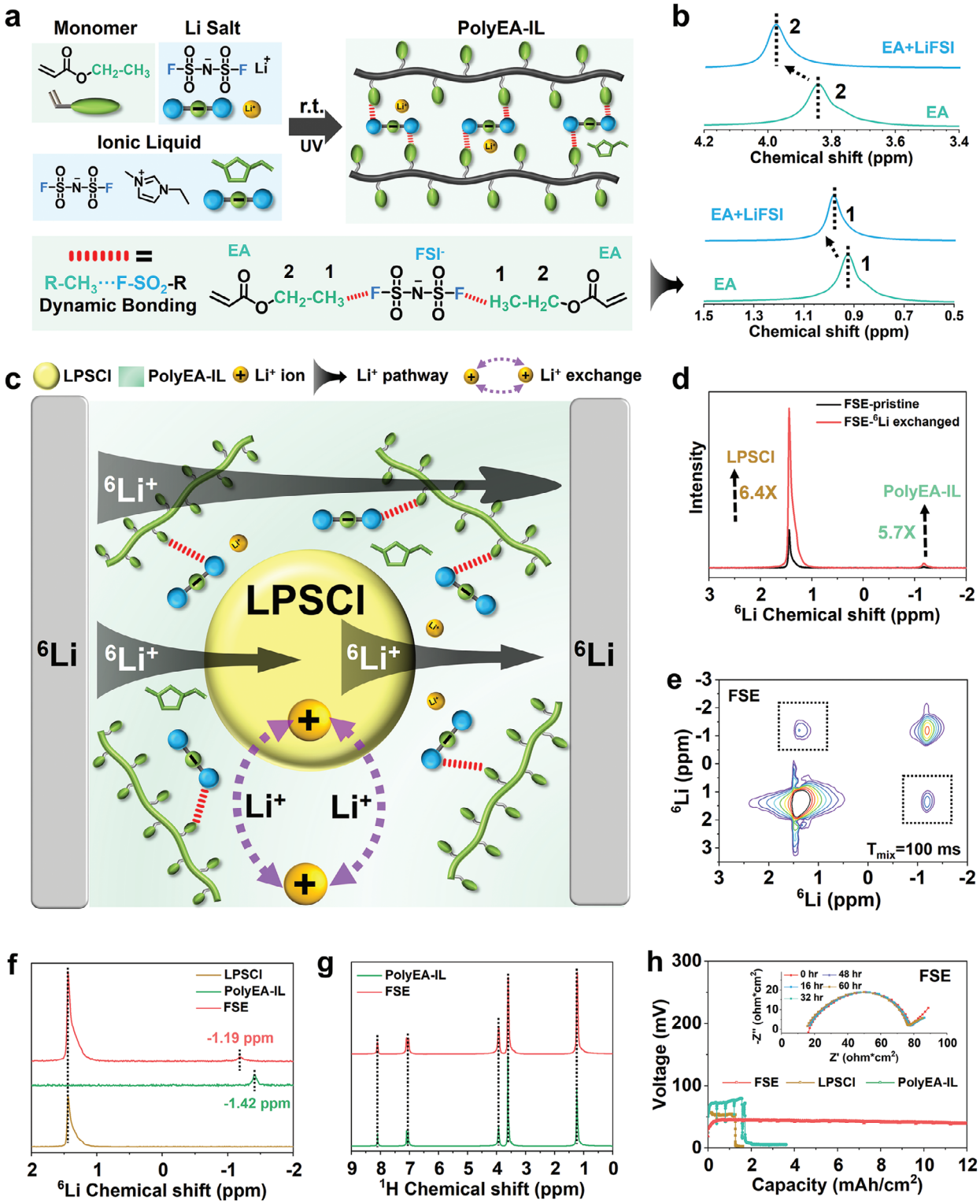

Figure 2. Solid-state NMR studies of synthesized electrolytes. a) Synthetic route of PolyEA-IL via a solvent-free, single-step UV-polymerization approach. b) Solid-state ^{1}H NMR spectra of ethyl acrylate monomer (EA) before and after introducing the LiFSI. c) Schematic illustration of proposed ion conduction pathway through the FSE electrolyte. d) 1D MAS ^{6}Li solid-state NMR spectra of pristine FSE (black line) and the FSE cycled in ^{6}Li-^{6}Li symmetric cells. The signal intensity was normalized by the sample mass and scanning number. e) ^{6}Li-^{6}Li 2D exchange spectroscopy (2D-EXSY) of FSE measured at r.t., spinning rate of 8 kHz, and mixing time of 100 ms. f) 1D MAS ^{6}Li solid-state NMR spectra of PolyEA-IL, LPSCl, and FSE. g) 1D MAS ^{1}H solid-state NMR spectra of PolyEA-IL and FSE. h) Short-circuiting time of Li^0/SSE/Li^0 cells. Inset shows the EIS evolution of Li^0/FSE/Li^0 cell with Li^0-deposition time at 30 °C.

interactions between Li^+ in PolyEA-IL and the surface groups of LPSCl crystals (e.g., tetrahedral PS_4^{3-}).[28]

To illustrate Li^+ transport through the stable polymer-ceramic interface, we monitored electrochemical impedance spectroscopy (EIS) during continuous Li^0 plating in a Li^0/FSE/Li^0 cell at 0.2 mA cm^{-2} (Figure 2h). Figure S7 (Supporting Information) further presents the equivalent circuit fitting results with bulk resistance (R_b) at 16 ohm cm^2, grain boundary resistance of LPSCl (R_{GB}) at 14 ohm cm^2, and charge transfer resistance (R_{CT}) at 46 ohm cm^2. During Li^0 deposition until 12 mAh cm^{-2}, the constant and low value of R_{gb} confirms the stable interphase between PolyEA-IL and LPSCl, consistent with the above NMR results. It is important to note that this R_{gb} does not appear in the EIS profile of the Li^0/ PolyEA-IL/Li^0 cell, and increasing the LPSCl ratio in FSE results in a higher R_{gb} for the Li^0/FSE/Li^0 cell (Figure S47, Supporting Information). In addition to the constant and low R_{gb}, the R_b and R_{CT} also remain constant, signifying the absence of dendrite penetration or electrode–electrolyte delamination. In contrast, Li^0–Li^0 cells with baseline LPSCl and PolyEA-IL experienced short-circuiting at 1.2 and 1.6 mAh cm^{-2}, respectively. The concentration polarization during the initial 0.4 mAh cm^{-2} in Li^0/PolyEA-IL/Li^0 cell was attributed to the low transference number of PolyEA-IL (0.31, Figure S36e, Supporting Information). Conversely, the high porosity of the LPSCl electrolyte (10.4%, Table S2, Supporting Information) results in elevated impedance and overpotential. In comparison, the FSE with PolyEA-IL as the continuous phase effectively infiltrates into the gaps and pores of LPSCl grains, leading to a low porosity of 4.14% (Table S2, Supporting Information). Meanwhile, the 66 wt% LPSCl as a conductive phase has contributed to an improved Li^+ transference number of 0.69 (Figure S36h, Supporting Information), thereby exhibiting lower overpotential compared to both PolyEA-IL and LPSCl. In addition, the capacity-voltage curve of Li^0/FSE/Li^0 also remains stable until charged to a high capacity of 12 mAh cm^{-2}. This enhanced dendrite-inhibiting ability of FSE can be attributed to its self-healing capability, unique mechanical properties, and stable interfacial chemistry, which will be discussed in the following sections.

2.2. Self-Healing Kinetics

Operando X-ray fluorescence (XRF) imaging technique was utilized to investigate the self-healing process. To accomplish this, we assembled in situ batteries with Li^0 and stainless steel electrodes in a Kapton tube (see the Experimental Section and Figure S8 in the Supporting Information for details) and obtained XRF images at 3000 eV to excite both sulfur (green) and phosphorus (red). Before cycling, two 50-µm voids were identified in the images as dark regions lacking both sulfur (S) and phosphorus (P) and were circled in white (**Figure 3a**). These voids, which are commonly observed in SCE-based batteries, are naturally formed during battery fabrication and are the hotspots for dendrite formation.[7–8,29] During cycling at 0.2 mA cm^{-2} and r.t., the voids gradually disappeared and the self-healed regions showed enriched levels of both S and P, indicating migration of both PolyEA-IL and LPSCl into the voids. Additionally, low-magnitude, large field-of-view XRF images confirm that most of the µm-sized cavities were repaired after 12 hours of battery operation (Figure S9, Supporting Information).

The S K-edge and P K-edge mappings, displayed individually in Figure S10 (Supporting Information), along with the quantitative analysis of the void size evolution in Figure 3c, provided insights into the self-healing kinetics. Notably, the self-healing process was found to accelerate with decreasing void size, with rates of 1.83 µm h^{-1} for a 37 µm void and 5.6 µm h^{-1} for a 28 µm void. Furthermore, the void size in the S mapping was consistently smaller than in the P mapping (P being a fingerprint of LPSCl), indicating the presence of an S-rich, P-deficient region between the void and bulk-SSE. This difference in healing states suggests a two-step self-healing process, in which PolyEA-IL infiltrates the void first, followed by the migration of LPSCl via the PolyEA-IL network to fill the void (Figure 3b). The in situ S K-edge X-ray absorption near edge spectroscopy (XANES) further confirms this mechanism (Figure 3d,e). The signal at 2469 eV is from the tetrahedral PS_4^{3-} in LPSCl,[30] while peaks at 2479 and 2480 eV are assigned to $-SO_2-$ in FSI^-,[31] which is the fingerprint of PolyEA-IL. At the bulk SSE, the unvarying spectra indicate a constant concentration of LPSCl and PolyEA-IL during battery operation (Figure S11, Supporting Information). However, within the void, non-normalized XANES (Figure 3d) shows increasing signal intensities for both LPSCl and PolyEA-IL, aligning with the observed self-healing process in XRF images. Furthermore, Figure 3e presents normalized X-ray absorption (xµE), revealing a decreasing relative intensity of the PolyEA-IL signal compared to the LPSCl signal over time, indicating LPSCl migration into the void subsequent to the infiltration of PolyEA-IL.

Using in situ, time-resolved TEM, we further validated the motion of LPSCl within the dynamic polymer matrix, supporting the above two-step self-healing kinetics. An in situ solid-state battery was created by connecting a Li^0-coated Cu tip to a FSE-coated W tip (Figure 3f, inset), and a voltage of 5 V was applied to initiate Li^0 deposition. In Figure 3f–h and Figure S12, Supporting Information, the shear displacement between two neighboring LPSCl particles during battery operation is demonstrated, and the surface profiles are depicted with a magenta dashed line. From 0 to 250 s, the edge of grain A gradually moves to the left, while after 250 s, the edge of grain B appears and moves upper right (the results can be best viewed in Movie S1, Supporting Information). The observed displacement between two grains is due to the movement of ceramics within PolyEA-IL, as both electrodes are kept stationary. The distance change between two LPSCl crystals is quantified in Figures S13 and S14 (Supporting Information), resulting in a displacement of ≈75 nm after 400 s, or a rate of 0.19 nm^{-1} s. Beyond enabling the two-step self-healing process, this electrolyte chemistry, characterized by mobile ceramic crystals within a dynamic polymer network, also facilitates the flowability of FSE and contributes to a stable interfacial chemistry, as detailed in the subsequent section.

2.3. Mechanical Properties and Interfacial Chemistry

The viscoelasticity of PolyEA-IL, depicted in **Figure 4a**, displays a unique liquid–solid transitioning properties,[32] transitioning from elastic solid behavior at short timescales to viscous flow at longer timescales.[33] For comparison, contrasting samples

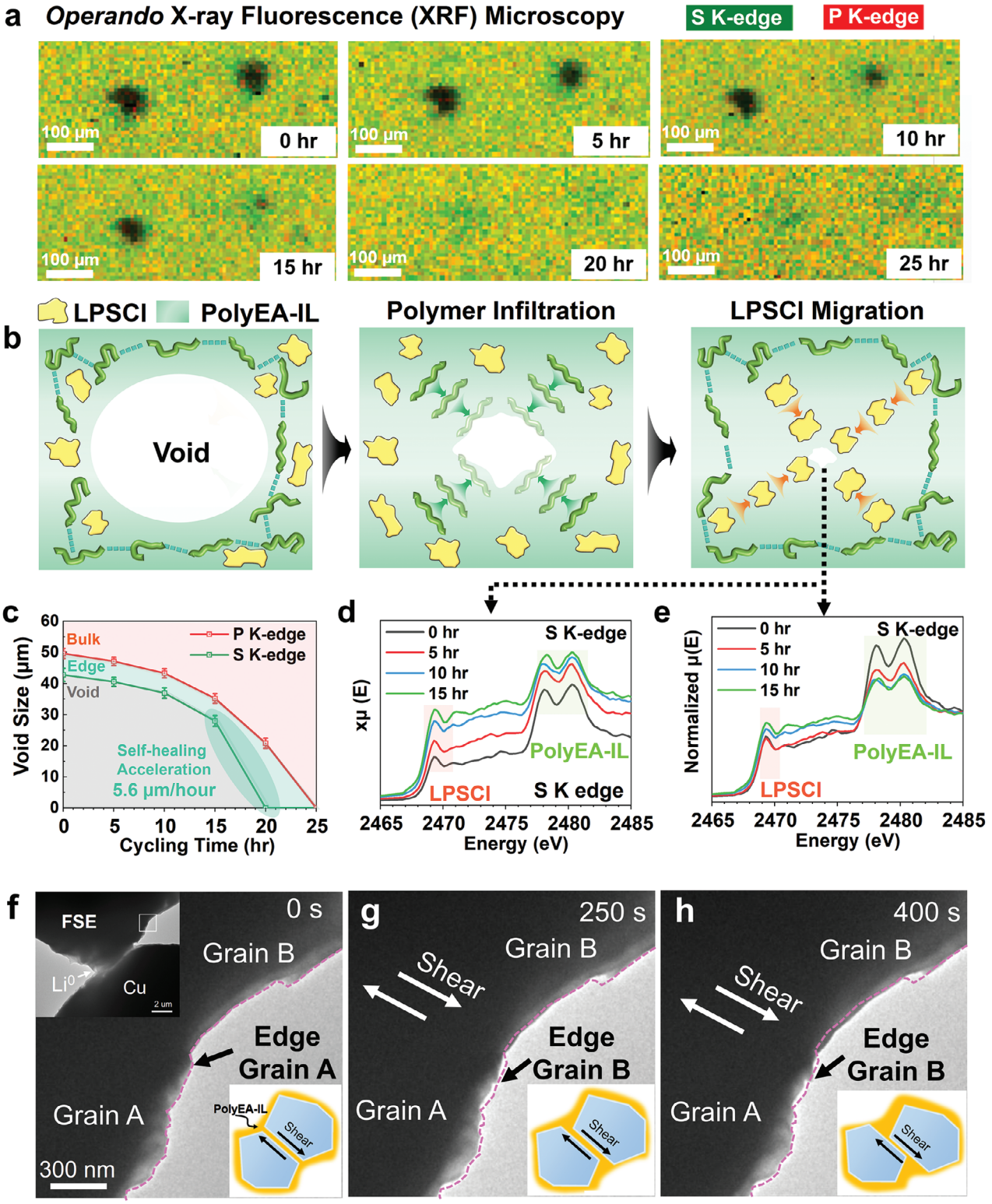

Figure 3. Self-healing kinetics revealed by operando XRF and in situ TEM. a) Time-resolved XRF mappings showing the self-healing kinetics. Note that we employed 2 mm thick SSE here to provide a large volume size for better observing the self-healing process. For battery testing, the SSE thickness is 350 μm (Figure S15, Supporting Information). b) Schematic illustration showing the two-step self-healing mechanism of FSE, in which PolyEA-IL infiltrates into voids first, followed by the migration of ceramic particles. c) Size evolution of the left void with cycling time revealing the two-step self-healing kinetics. d,e) Evolution of non-normalized d) and normalized e) S K-edge XANES spectra within the void. f–h) Time-resolved in situ TEM images during Li^0-deposition showing the shear displacement between two neighboring LPSCl particles.

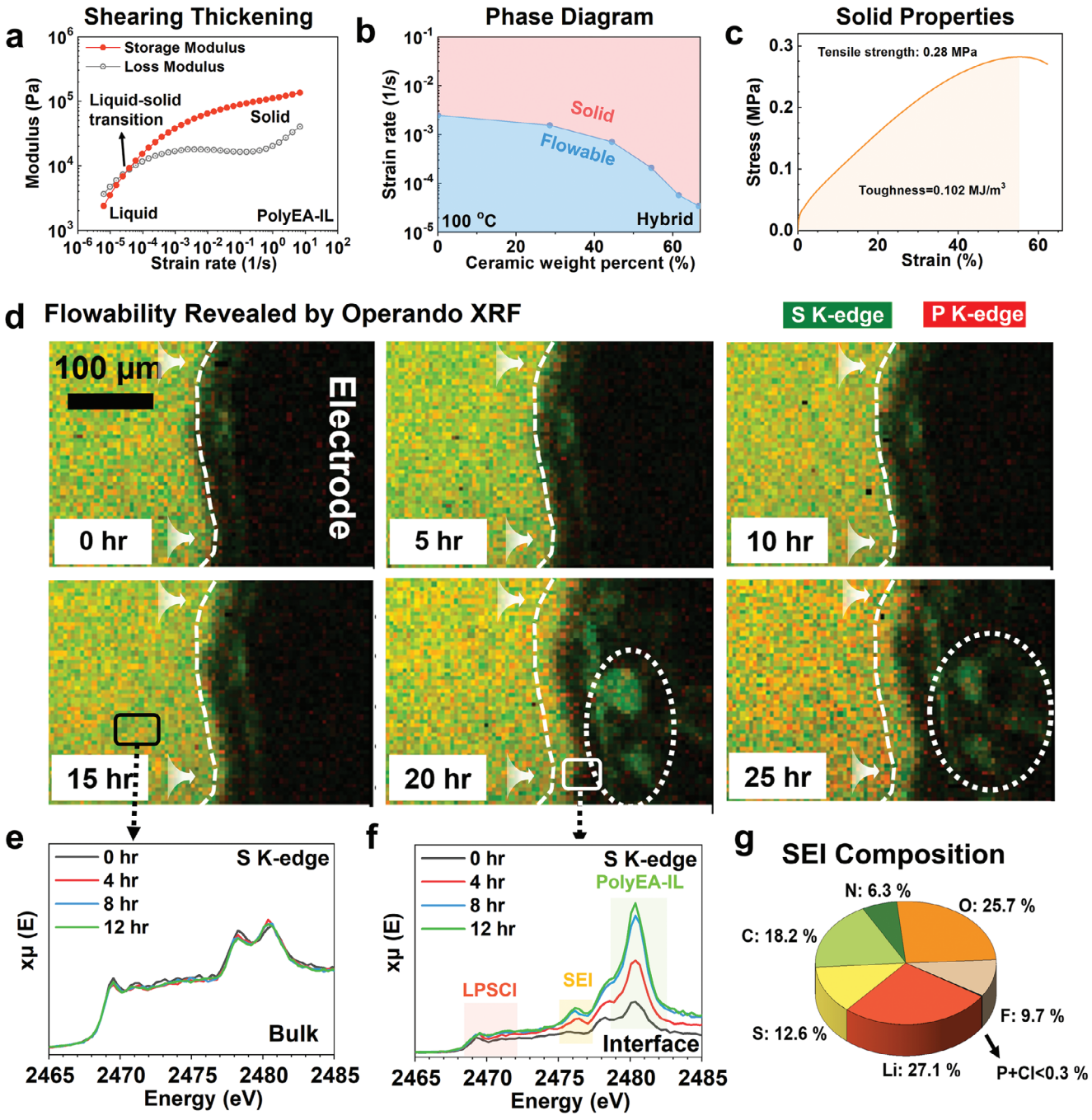

Figure 4. Mechanical properties and flowability. a) Viscoelastic properties of PolyEA-IL measured by rheometer at 30 °C. b) Dynamical phase diagram of FSE showing the effect of ceramic concentration on the liquid-solid properties. c) Stress–strain curves of FSE showing its solid properties with a tensile stress of 0.28 MPa. d) Overlaid S K-edge and P K-edge XRF images at the electrode–electrolyte interface during cycling at 0.2 mA cm^{-2} and r.t. The white dashed line indicates the original position of the electrolyte-electrode interface. e,f) Evolution of non-normalized S K-edge XANES spectra at the bulk SSE e) and interface area f). g) XPS quantitative analysis showing the atomic composition of FSE-derived SEI on a Cu foil.

without dynamic bonding maintain a liquid state, as evidenced by consistently higher loss modulus (G'') than storage modulus (G') (Figure S16a,b, Supporting Information). While the sample with permanent covalent crosslinking behaves as an elastic solid (Figure S16c, Supporting Information), characterized by a low loss factor of ≈0.2 ($\tan\delta = G''/G'$). This suggests that the liquid-solid transitioning properties observed in PolyEA-IL, similar to findings in previous dynamic polymers,[34] can be attributed to the dynamic bonding and the high segmental mobility of polymer chains (T_g = −56 °C, Figure S12c, Supporting Information). At low strain rates (longer time scales), dynamic bonds constantly undergo break-reform cycles, allowing highly mobile

polymer chains to flow like a liquid over time (Figure S16d, Supporting Information).[35] However, at higher strain rates, the dynamic bonding may not have sufficient time for transient cleavage, resulting in a significant increase in the storage modulus and solid-like behavior.[36] This liquid-solid property enables the cold-milling fabrication of FSE and also facilitates the infiltration of PolyEA-IL into voids, thus promoting the self-healing process.

After hybridization with LPSCl, FSE retains the liquid-solid phase-transition behavior, as demonstrated by its viscoelastic properties (Figure S17, Supporting Information). Additionally, the dynamical phase diagram for FSE (Figure 4b) reveals a significant decrease in phase transition strain rate as the ceramic mass ratio increases, owing to particle-particle interactions that enhance material rigidity.[37] In practical SSLMB applications, Li^0 plating/stripping occurs within a 36000-s timeframe at C/10 (i.e., strain rates of 10^{-5} s^{-1}). To match this relevant timescale, we use a formulation with 66 wt% ceramic. This enables the FSE to possess both flowability during Li^0 stripping (low strain) to infiltrate and repair the voids, as well as elastic solid properties during Li^0 plating (high strain) to inhibit dendrites. The stress-strain curves in Figure 4c indicate a high tensile strength of 0.28 MPa, while the rheology test in Figure S17 (Supporting Information) shows a storage modulus of 1.4 MPa, confirming FSE's elastic–solid properties for regulating Li^0 deposition. Additionally, Movie S2 (Supporting Information) demonstrates FSE's ability to withstand a hammer shock test without visible cracks or damage, highlighting its superior resilience compared to traditional SCEs. Figure S18 (Supporting Information) further compares the modulus of various SSE classes. The high elastic modulus of SCEs (30–140 GPa) surpasses the Monroe–Newman prediction.[3] however, short-circuit-induced cell failures are still commonly observed due to the inevitable formation of voids and cracks.[8,38] Meanwhile, semi-solid polymer electrolytes offer better interfacial contact but are more susceptible to dendrite penetration due to their inadequate modulus (<10 kPa).[39] The modulus-density scaling relationship, expressed as $E/E_s \sim (\rho/\rho_s)^{3.6}$,[40,41] predicts an effective modulus of 0.85 MPa for mossy Li^0 with 90% porosity. Once mossy Li^0 (i.e., Li^0 whisker or Li^0 dendrites) forms, its growth will be mechanically limited and impeded by the high modulus FSE. As a result, the Li^0 structure is expected to evolve into increasingly uniform, dense, and compact forms, thereby effectively regulating the deposition behavior of Li^0.[41]

The flowability of FSE was demonstrated by *operando* XRF monitoring at the electrode–electrolyte interface (Figure 4d and Figure S19, Supporting Information). During cycling at 0.2 mA cm^{-2} for 25 h, we observed no cracking or delamination, in contrast to SCE-based batteries.[7,29] Instead, FSE migrated and spread over the electrode surface at a rate of 1.33 µm h^{-1} (Figure S20, Supporting Information), adapting to the moving Li^0 interface and accommodating volume changes during plating and stripping. Consistent with the dynamical phase diagram in Figure 4b, FSE with a reduced ceramic loading of 60 wt% demonstrated improved flowability of 3.58 µm h^{-1} (Figures S21 and S22, Supporting Information). This increased flow rate also enhanced self-healing kinetics by facilitating FSE infiltration into voids. As shown in Figure S23 (Supporting Information), voids as large as 70 µm were completely repaired within 15 hours during battery operation. Additionally, FSE exhibited a notable adhesive energy of 65.5 J m^{-2} to copper foil(Figure S24, Supporting Information), further contributing to interface stability and preventing delamination.[42]

The chemical evolution at the electrode–electrolyte interface was monitored by in situ XANES. Figure 4e,f present the variation of X-ray absorption (xµE). During cycling, the S K-edge XANES at the bulk FSE remained unchanged (Figure 4e). However, at the interface (Figure 4f), the increased signal intensity at 2469 and 2480 eV indicates higher concentrations of LPSCl and PolyEA-IL, confirming FSE's flowability. In the normalized xµE profile (Figure S25, Supporting Information), we observed an increasing PolyEA-IL to LPSCl ratio during cycling, indicating the enrichment of PolyEA-IL at the interface. This further prevents LPSCl degradation, as evidenced by the well-maintained peak shape and pre-edge energy at 2469 eV. In contrast, pristine LPSCl experiences a shift in pre-edge energy from 2469 to 2471 eV (Figure S26, Supporting Information), indicating reduction to Li_2S. Figure 4f also presents evidence of a PolyEA-IL-derived SEI, confirmed by the peak that emerged at 2476 eV after 4 h, which is attributed to the $-SO_x-$ reduced from $-SO_2-$ in FSI^-.[31,43] (ex situ XANES exhibits a similar trend, Figure S27, Supporting Information). The SEI chemistry was also analyzed by X-ray photoelectron spectroscopy (XPS) (Figure S28, Supporting Information). The presence of $-SO_x-$ signals at 167 eV confirms the in situ XANES results. Additionally, the SEI contains LiF, Li_3N, Li_2O, Li_2CO_3, and Li_2S, resulting from the electrochemical reduction of PolyEA-IL. Notably, no P/Cl signals were detected, and XPS quantification indicated that the atomic ratio of P+Cl was <0.3% (Figure 4g), highlighting a stable interfacial chemistry that minimized the degradation of LPSCl and imidazolium cations.

2.4. Compatibility in Li^0 Anode Batteries

The capability of FSE to regulate Li^0 deposition was demonstrated by cryo-TEM characterization. **Figure 5**a shows uniform, dome-shaped Li^0 deposits that are intimately protected by a dense and compact SEI layer (indicated by the dashed lines in the inset). Figure 5b shows a representative selected-area electron diffraction (SAED) of the deposited Li^0, where a pair of Bragg spots can be assigned to the (112) plane of body-centered cubic Li^0 (Li^0 bcc). The atomic structure of the Li^0-deposit and SEI is shown in Figure 5c, where the SEI comprises nano-sized crystals (e.g., Li_2O indicated by dashed circles) with varied crystallographic orientations. The polycrystal ring in the fast Fourier transform (FFT) in the inset corresponds to the Li_2O (111) planes. This SEI intimately protects the deposited Li^0 and separates it from the electrolyte to minimize the decomposition of LPSCl and imidazolium cation. The above cryo-TEM finding is also consistent with the SEM characterization, which reveals a dendrite-free, uniform, and smooth morphology of deposited Li^0 under the FSE (Figure S30, Supporting Information). As discussed above, this formation of dense, bcc-structured Li^0 could be attributed to the solid properties of the FSE, characterized by a modulus in the MPa range, which prevents the formation of mossy or dendritic Li^0. Attributing to the good dendrite-inhibiting ability, the Li^0/FSE/Cu cell shows stable operation over 700 cycles at 0.2 and 0.5 mAh cm^{-2}, with an average coulombic efficiency of 99.1% during cycles 500^{th} to 700^{th} (Figure S43, Supporting Information). The observed 0.9% coulombic inefficiency may

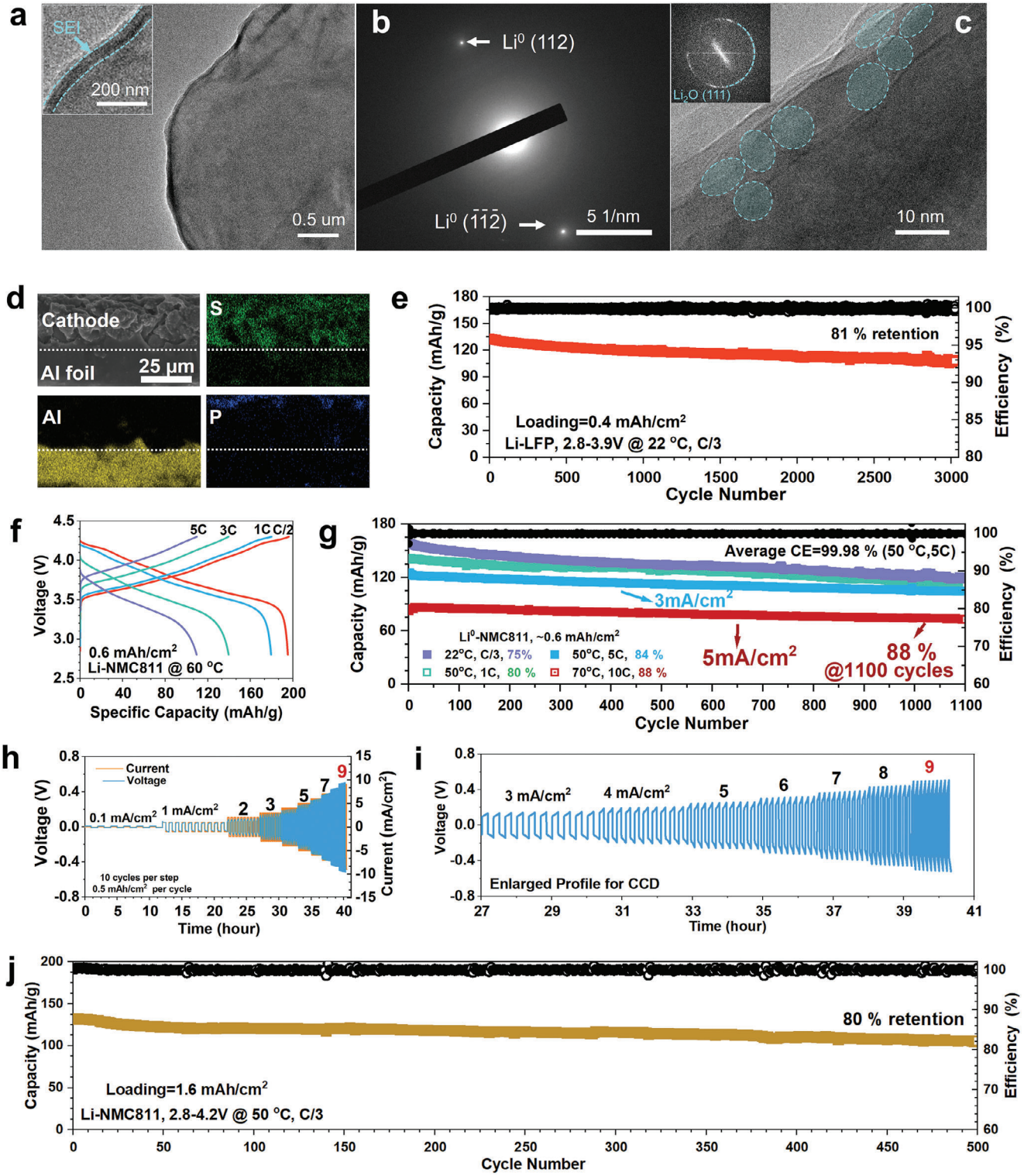

Figure 5. Compatibility in Li^0-anode batteries. a) Cryo-TEM images showing the morphology of the deposited Li^0 under FSE. b) Electron diffraction pattern (EDP) of the deposited Li^0. c) Atomic-resolution cryo-TEM image showing the structure of the Li^0-deposit and SEI. d, SEM-EDS mapping of cycled NMC811 cathode under FSE. e) Li^0-$LiFePO_4$ battery performance at r.t. f, Rate capability of Li^0-NMC811 cell. g) Long-term cyclability of Li^0-NMC811 cell at 50 °C and r.t. h) Critical current density of Li^0/FSE/Li^0 cell measured at 50 °C. i) Enlarged voltage-time curves showing there is no short-circuiting during the CCD measurement. j) Performance of SSLMB employing commercial high-loading NMC811 cathode. Full cells were activated at 0.1C for two cycles to allow the formation of stable SEI, and the charge-discharge curves are shown in Figure S38 (Supporting Information).

be ascribed to dead Li^0 formation or side reactions. For comparison, the Li^0/LPSCl/Cu cell exhibited low coulombic efficiency of 20–70% and failed after 6 cycles due to short-circuiting (Figure S27a, Supporting Information). As well-documented, this failure is caused by local current density concentration.[7] and crack-tip-stresses-induced crack propagation.[8,29] Furthermore, the Li/PolyEA-IL/Cu cell also displayed low coulombic efficiency (≈80%) and limited cycling life (160 h, Figure S27c, Supporting Information).

Full cells with Li^0 anodes were then assembled. To prevent LPSCl degradation at high potentials,[44] we implemented a Janus electrolyte architecture with LPSCl-based FSE on the anode side and LATP-based FSE on the cathode side. Figure 5d depicts SEM-EDS mapping of a 30-µm thick NMC811 cathode cycled under FSE. The uniform distribution of S elements within the cathode layer suggests the infiltration of PolyEA-IL into the cathode pores, creating an ion conduction pathway. This compatibility with existing cathode fabrication techniques eliminates the need for introducing a solid ion conductor,[31] or reducing carbon content,[45] in the cathode. We first paired the FSE with a low-cost and high-safety $LiFePO_4$ cathode. Figure 5e illustrates exceptional cycling durability, enduring over 3000 cycles at C/3 (>14 000 h), while maintaining 81% of its initial capacity, indicating a minimal decay rate of 0.0062% per cycle. When employing high-voltage NMC811 cathodes, the cell exhibited good rate capability, delivering specific capacities of 195 mA g^{-1} at 0.5C and 118 mAh g^{-1} at 5C (Figure 5f). At room temperature and C/3, the capacity retention after 1100 cycles reached 75%. After operating at 1C and 50 °C for 1100 cycles, the Li-NMC811 cell maintained 80% of its initial capacity with an average coulombic efficiency of 99.96% (Figure 5g). Attributed to the high critical current density of FSE (9 mA cm^{-2}, Figure 5h,i), Li-NMC811 exhibits stable cycling even at a high current density of 5C (3 mA cm^{-2}), retaining 84% capacity after 1100 cycles, with an average coulombic efficiency of 99.98%. At 5 mA cm^{-2}, the capacity retention is 88% after 1100 cycles.

Figure 5j further shows cycling performance with a high-loading commercial NMC811 cathode (1.6 mAh cm^{-2}). The cell maintained stability over 500 cycles with 80% capacity retention. Smooth charge-discharge curves in Figure S31 (Supporting Information) indicated no soft-shorting, while a high average coulombic efficiency of 99.96% confirmed a stable interface with both the cathode and anode. Notably, these tests were conducted with pristine Li^0 anodes, near-zero stack pressure (0.1 MPa in coin cells), and no catholyte addition. In Figure S32 and Table S1 (Supporting Information), we compared the performance of FSE with previous composite electrolyte systems. The results highlight that FSE has improved compatibility with Li^0 anodes, extended cycling life, and enhanced areal capacity. These advancements originate from its innovative electrolyte chemistry, combining self-healing capability, flowability, and solid properties.

3. Conclusion

In this study, we have developed an innovative electrolyte chemistry featuring unconstrained ceramic conductors within a dynamic polymer network. Through operando imaging techniques of TEM and XRF, a two-step self-healing mechanism was revealed, leading to the complete healing of defective voids at a rapid rate of 5.6 µm h^{-1}. The chemistry at the polymer-ceramic interphase was elucidated via solid-state NMR, revealing rapid Li^+ diffusion that facilitates a dual-phase ion conduction pathway. Simultaneously, in situ XANEs monitoring unveiled a stable polymer-derived SEI, which stabilizes the electrode–electrolyte interface and mitigates electrolyte degradation. Benefiting from the liquid-solid transitioning properties of dynamic polymer, the FSE manifests both solid characteristics and flowability on relevant timescales, displaying solid properties with a tensile strength of 0.28 MPa while remaining flowable at a rate of 1.33 µm h^{-1}. When incorporated into a solid-state Li^0 battery, this electrolyte offers a combination of attributes: self-healing capability to address mechanical instability, flowability ensuring intimate interface contact, and an MPa-level elastic modulus to regulate Li^0 deposition. Overall, this study pioneers new methodologies for visualizing and optimizing chemical processes and ion transport at material interfaces and interphases. Its design concept might inspire battery communities to tackle practical interfacial challenges and dendrite formation issues, by leveraging advanced polymer chemistry to integrate seemingly conflicting material traits, such as flowability and solid properties.

4. Experimental Section

Materials: Ethyl acrylate (EA) and 4-fluoro-1,3-dioxolan-2-one (FEC) were purchased from Sigma-Aldrich and used as received. Phenylbis-(2,4,6-trimethyl benzoyl)-phosphineoxide (BAPO), and lithium bisfluoro sulfonyl imide (LiFSI), were purchased from TCI. 1-Ethyl-3-methyl imidazolium bis(fluoro sulfonyl)imide (EMIMFSI) was purchased from Solvionic and used as received. Li_6PS_5Cl (LPSCl) and $Li_{1.3}Al_{0.3}Ti_{1.7}(PO_4)_3$ (LATP) with particle size ≈1 µm were purchased from NEI Corporation and used as received. The LPSCl baseline electrolyte was prepared by a cold-pressing process at 150 MPa, and the thickness is ≈800 µm.

Synthesis of the Dynamic Polymer (PolyEA-IL): A solvent-free, single-step UV polymerization method was employed for the synthesis of PolyEA-IL. To enhance the chain mobility of the polymer backbone and facilitate lithium salt dissociation, EMIMFSI ionic liquid as a plasticizer is introduced. This ionic liquid, often referred to as a room-temperature molten salt, possesses nonflammability and nonvolatility characteristics, thus mitigating potential safety concerns in solid-state batteries. EA was chosen as the monomer due to its inherent capacity to establish dynamic bonding between the $–CH_2–CH_3$ and $SO_2–F$ groups,[18] endowing PolyEA-IL with self-healing capabilities. Furthermore, FEC was incorporated as an additive, owing to its extensively documented capacity to induce the formation of a robust SEI layer on the Li^0 anode.

Experimental procedure: A solvent-free liquid precursor was prepared by stirring a mixture of LiFSI (0.3 g), EA (0.2 g), EMIMFSI (0.5 g), and FEC (50 mg, 5 wt%) for 30 min, resulting in a transparent solution. The photoinitiator (BAPO, 0.1 wt%) was then added and stirred for an additional 5 min. This solution was subsequently cast onto a smooth glass plate and exposed to 365 nm UV light for 15 minutes. The resulting PolyEA-IL was stored in an Ar-filled glove box before use. The thickness of the PolyEA-IL baseline electrolyte was controlled to match that of the FSE (350 µm).

Monomer conversion yield: The monomer conversion yield during UV polymerization was assessed using solid-state ^1H NMR spectroscopy. In the ^1H NMR spectrum of EA (Figure S12a, Supporting Information), signals 3–5 at 5.5–6.5 ppm corresponded to protons on the C=C double bond. In the NMR spectra of PolyEA-IL, no signals were detected between 6-6.5 ppm, indicating a nearly quantitative monomer conversion yield of ≈100%.

Effect of ionic liquid content: Increasing the content of ionic liquid (IL) enhances the room temperature performance of batteries. When the IL ratio in PolyEA-IL was increased to 66 wt% (i.e., 22 wt% in FSE), the T_g decreased from −55.6 to −71.6 °C (Figures S40a and S40b, Supporting

Information), improving the ionic conductivity of FSE (1.9 mS cm^{-1} vs 1.5 mS cm^{-1} at 30 °C, Figure S40c,d, Supporting Information). As a result, the Li^0//FSE//NMC811 cell delivered a high specific capacity of 172.4 mAh g^{-1} when operating at 0.5 C and room temperature (Figure S39, Supporting Information). In contrast, the original formulation (50 wt% IL in PolyEA-IL) delivered a much lower capacity of ≈132.9 mAh g^{-1}. However, increasing IL content also decreased the mechanical properties of PolyEA-IL. The storage modulus dropped ≈10-fold from 10^4–10^5 to 10^3–10^4 Pa, and the phase transitioning strain rate increased from 3.00E−05 s^{-1} to 4.33E−04 s^{-1}, indicating a more liquid-like behavior (Figure S41, Supporting Information). These changes resulted in inferior cycling life and stability, with 64% capacity retention after 800 cycles at 66 wt% IL compared to 72% retention after 1000 cycles at 50 wt% IL. To balance capacity and cycling stability, an optimal formulation with 50 wt% IL in PolyEA-IL was adopted.

Synthesis of the Flowable Yet Solid Electrolyte (FSE): Synthesis: The FSE was prepared using a straightforward cold-milling process. In this method, PolyEA-IL (33 wt%) and ceramic electrolyte (LPSCl or LATP, 67 wt%) were combined in an agate mortar and milled at room temperature for 30 min. To ensure a uniform dispersion of the ceramic within the PolyEA-IL matrix, the resulting FSE was subsequently subjected to roll-pressing to form a thin membrane. This membrane was then folded and roll-pressed repeatedly. The resulting FSE film was then punched into 12-mm-diameter discs and stored in an Ar-filled glove box prior to use. This cold-milling fabrication process offers the advantage of avoiding the complex high-temperature, high-pressure, press-sintering methods typically employed in conventional SCE fabrication approaches.

Conductivities: Figure S33 (Supporting Information) illustrates the ionic and electron conductivities of the FSE. High ionic conductivity (1.5 mS cm^{-1} at 30 °C) and low electron conductivity (2.73 × 10^{-10} S cm^{-1}) were realized, primarily due to the intimate PolyEA-IL coating on LPSCl (140 nm-thick, as depicted in Figure S34, Supporting Information). This coating facilitates particle-to-particle ion conduction while obstructing the electron conduction pathway.

Electrolyte thickness: For battery performance testing, the FSE thickness was 350 µm (see Figure S11 in the Supporting Information). To prepare the Janus electrolyte for full cell testing, a 120 µm LPSCl-based FSE was positioned facing the Li^0 anode, while a 230 µm LATP-based FSE was employed facing the cathode. Consequently, the total electrolyte thickness is ≈350 µm. For XRF measurement, a 2-mm thick FSE was utilized to provide a larger volume size for better observation of the self-healing mechanism.

To demonstrate the potential of the electrolyte to deliver stable long-term cycling performance at reduced thicknesses, we further fabricated a 140-µm FSE, and the Li^0-Li^0 cell performance is presented in Figure S37 (Supporting Information). The cell has operated stably for 5400 h at 0.2 mA cm^{-2}, 0.5 mAh cm^{-2}, and room temperature. When employing this 140-µm FSE, the Li^0-Li^0 cell exhibits a high critical current density of 9 mA cm^{-2} (Figure 5h). Additionally, a 140-µm Janus electrolyte was fabricated, with the thicknesses of the LATP-based FSE and LPSCl-based FSE being ≈90 and ≈50 µm, respectively. Li^0-NMC811 cells employing this 140-µm Janus electrolyte operated stably at 4.6 mA cm^{-2} for 1000 cycles with 90% capacity retention (Figure S48, Supporting Information).

Density and Pore Volume of Electrolyte: The pore volume of FSE was determined based on the densities of its constituent electrolyte components, as detailed in Table S2 (Supporting Information). The documented theoretical density of LPSCl is 1.64 g cm^{-3} (ρ_1).[46] Meanwhile, the measured densities of LPSCl powder (ρ_2) and PolyEA-IL polymer (ρ_3) were 0.90 and 1.46 g cm^{-3}, respectively. Following the cold milling process (with a mass ratio of 2:1 between LPSCl and PolyEA-IL), the density of FSE (ρ_4) was determined to be 1.51 g cm^{-3}. Consequently, the porosity of FSE was calculated using the formula 1-ρ_4/ρ_3/3-2×ρ_4/ρ_1/3, resulting in a porosity of 4.14%. For LPSCl powder, the porosity of was calculated as 45.1% using the formula 1-ρ_2/ρ_1. This calculation yields a pore-filling degree of 90.8% after cold-milling of LPSCl powder and PolyEA-IL.

To provide a basis for comparison, the density of an LPSCl pellet fabricated through cold-pressing at 150 MPa was determined to be 1.47 g cm^{-3}, corresponding to a porosity of 10.4%, significantly higher than that of FSE (4.14%). Consistent with the measured low porosity of FSE, SEM characterizations reveal a homogeneous distribution of LPSCl particles within the polymer matrix (see Figure S35 in the Supporting Information). High-resolution cryo-TEM images further confirm that LPSCl is uniformly coated by a polymer layer with an approximate thickness of 0.14 µm (see Figure S34 in the Supporting Information).

Electrode Preparation and Battery Assembling: $LiFePO_4$ and $LiNi_{0.8}Mn_{0.1}Co_{0.1}O_2$ cathodes were fabricated via the conventional slurry-casting procedure. Typically, superP (20 mg) and active material (160 mg) were hand-milled in an agate mortar for ≈10 min. Afterward, 20 mg PVDF binder (8 wt% dissolved in NMP) was added, and the mixture was mixed with a Thinky Mixer for 15 min. The obtained slurry was blade-casted onto aluminum foil and dried at 85 °C under vacuum. The commercial high-loading $LiNi_{0.8}Mn_{0.1}Co_{0.1}O_2$ cathode (1.6 mAh cm^{-2}) was obtained from the Cell Analysis, Modeling, and Prototyping (CAMP) Facility. Li^0 foil with a thickness of 250 µm was employed as the anode. The areas of the Li^0 anode, LFP cathode, and NMC811 cathode are 1.13 cm^2, with a corresponding diameter of 1.2 cm. 2032 coin cells were assembled inside an Ar-filled glove box (H_2O < 1 ppm, O_2 < 0.1 ppm), and cycled using a NEWARE multichannel cycler. Electrochemical properties were measured on a Biologic EC-Lab electrochemical station. Li^0–Li^0 cells were tested at r.t. and under low stack pressure in coin cells. The Li^0–Li^0 cells were activated at 0.1 mA cm^{-2} for ≈20 hours before cycling at 0.2 or 0.5 mA cm^{-2}. The critical current density (CCD) was measured at a current step of 1 mA/cm^2, with 10 cycles for each current density. The thickness of employed FSE for CCD measurement is 140 µm. Full cells were activated at 0.1C for two cycles before operation at higher C-rates. To evaluate the cycling stability at high current densities, the Li^0-NMC811 cells was tested at 50 or 70 °C to decrease the interfacial resistance between FSE and Li^0 anode. Figure S42 (Supporting Information) shows the EIS evolution of the Li^0/FSE/Li^0 cell with increasing temperatures. At 30, 50, and 70 °C, the charge transfer resistance is 47, 37, and 19 ohm cm^{-2}, respectively. Also attributing to the increased conductivity and decreased grain boundary resistance, the overall resistance of the cell decreased from 78 ohm×cm^2 to 56 ohm×cm^2 to 33 ohm×cm^2 as the temperature increased from 30 to 70 °C.

Electrochemical Characterization: Electronic conductivity was measured by applying a constant voltage of 150 mV on an SS/SSE/SS cell (SS refers to stainless steel). Ionic conductivity and charge transfer resistance of electrolytes were measured by electrochemical impedance spectroscopy (EIS) under the cell configuration of SS/SSE/SS and Li/SSE/Li, respectively. The frequency range is 3 MHz to 1 Hz and the polarization voltage is 5 mV. Ionic conductivities (σ_{ion}) were calculated based on Equation (1)

$$\sigma_{ion} = d/(R \cdot S) \quad (1)$$

where R (ohm) is the measured resistance from EIS profiles. S (cm^2) and d (cm) are the area and thickness of employed SSEs.

Material Characterization: The viscoelasticity of FSE was measured by a TA DHR-2 rheometer under the oscillation mode using a parallel plate setup. The diameter of the plate is 20 mm, and the frequency sweep was performed at the fixed strain of 1%. The storage modulus (G'') and loss modulus (G') represent the elastic and viscous properties of materials, respectively. The tensile strength and surface adhesion energy were measured with a dynamic mechanical analyzer (DMA-Q800, TA Instruments). The glass transition temperature was measured by differential scanning calorimeter (DSC 2500, TA Instruments) at a temperature ramp rate of 5 °C/min. SEM characterization was conducted using a LEXI-FEI Magellan400. Kratos AXIS-Supra was employed to record the X-ray photoelectron spectroscopy (XPS) profiles. All XPS samples were transferred under an inert atmosphere through an Ar-filled glove box.

Tender Energy X-ray Fluorescence (XRF) Microscopy and XANES Characterization: XRF microscopy and XANES experiments were performed at beamline 8-BM of the National Synchrotron Light Source II (NSLS II) at Brookhaven National Laboratory. A tube-geometric was employed to fabricate the in situ batteries (Figure S4, Supporting Information). Li^0, FSE, and stainless steel rod were employed as the reference electrode, solid electrolyte, and working electrode, respectively, and installed inside a

2-mm diameter Kapton tube. Both ends of the Kapton tube were well-sealed with epoxy to minimize air exposure. The tube battery samples were sealed inside an aluminum-coated plastic bag before use and were quickly transferred to a He-filled chamber for XRF and XANES measurements.

Solid-State NMR: Solid-state NMR experiments were conducted using a Bruker Avance 500 spectrometer with a magnetic field strength (B_0) of 11.7 T. A Bruker double-resonance MAS probe was employed for all experiments. The Larmor frequencies for the ^{1}H, ^{7}Li, and ^{6}Li nuclei were 500.130, 194.37, and 73.6 MHz, respectively. In the case of ^{7}Li and ^{6}Li experiments, calibration of the spectrometer was done relative to a 1 M LiCl solution (set at 0 ppm). For ^{1}H experiments, chemical shifts were referenced against tetramethylsilane (TMS) (^{1}H at 0 ppm), and the samples were measured successively under identical experimental setup, with each ^{1}H spectrum comprising 32 scans (≈2 min). Samples were packed in a 4 mm diameter ZrO_2 rotor, and the spinning rate was set at 8000 Hz. To investigate the ion conduction pathway, ^{6}Li isotope exchange experiments were conducted. The FSE electrolyte was cycled in a ^{6}Li-^{6}Li symmetric cell for 160 h to replace the $^{7}Li^{+}$ ions with $^{6}Li^{+}$ ions. Subsequently, the cell was disassembled, and the FSE electrolyte was packed into the ZrO_2 NMR rotor inside the glove box. The signal intensity of the obtained ^{6}Li spectrum was normalized by the sample mass and the number of scans, and then compared with that of the pristine FSE.

Cryo-TEM and In Situ TEM Experiment: The cryogenic transmission electron microscopy (cryo-TEM) experiments are performed by using a double-tilt liquid nitrogen cryo-transfer holder (Model 915) with a specially designed anti-frost shutter. The samples are transferred at the liquid N_2 temperature. The cryo-TEM experiments are conducted on a JEOL 2100F (acceleration voltage 200 KV) or GrandArm300 microscope (acceleration voltage 300 KV). The cryo-TEM samples are prepared by inserting a 200 mesh copper grid onto the copper electrode in a coin cell. The battery assembly is operated in a glove box with argon protection. The Li^0 deposition is performed in a NEWARE battery testing system, at a current density of 0.2 mA cm^{-2} and discharge time of 2.5 h. At the end of Li^0 deposition, the coin cells are disassembled and the Cu grids are sealed in an aluminum pouch bag in a glove box. On site of the TEM experiment, the pouch bag is plunged into a liquid N_2 for precooling. Next, the precooled Cu grids are transferred into the liquid bath in the holder stand and then fixed onto the holder tip for further cryo-TEM characterization.

The in situ TEM experiment is performed in an FEI Talos F200X transmission electron microscope (acceleration voltage 200 kV) using a Nanofactory STM-TEM probing system. To construct a micro battery in the microscope, the solid-state electrolyte particles are inserted between two electrodes, i.e., a copper electrode and a tungsten (W) probe covered by a scratch of Li^0. A voltage of 5 volts is applied for the in situ Li deposition through the solid-state electrolytes. Note that the voltage applied here is slightly higher than that in real batteries because of a point contact resistance between the solid-state electrolyte and the Li^0 anode.

Supporting Information

Supporting Information is available from the Wiley Online Library or from the author.

Acknowledgements

Y.H. and C.W. contributed equally to this work. This work was primarily supported by the Assistant Secretary for Energy Efficiency and Renewable Energy, Vehicle Technology Office of the U.S. Department of Energy (DOE) through the Advanced Battery Materials Research Program under contract no. DE-SC0012704. The Cryo-EM characterization was supported by the Office of Basic Energy Sciences of the U.S. Department of Energy, under award no. DE-SC0021204. This work made use of facilities and instrumentation at the UC Irvine Materials Research Institute (IMRI), which is supported in part by the National Science Foundation through the UC Irvine Materials Research Science and Engineering Center (DMR-2011967). JL acknowledges support by DARPA MINT program under contract number HR001122C0097. XPS work was performed using instrumentation funded in part by the National Science Foundation Major Research Instrumentation Program under grant no. CHE-1338173. This research used resources from the Center for Functional Nanomaterials (CFN), which is a U.S. Department of Energy Office of Science User Facility, at Brookhaven National Laboratory under Contract No. DE-SC0012704. The authors would like to acknowledge the ANL CAMP facility for providing the electrodes. The CAMP Facility is fully supported by the DOE Vehicle Technologies Office. This research used beamline 8-BM of the National Synchrotron Light Source II, a U.S. Department of Energy (DOE) Office of Science User Facility operated for the DOE Office of Science by Brookhaven National Laboratory under Contract No. DE-SC0012704. The authors acknowledge Dr. Seong-Min Bak and Yonghua Du for their contribution and suggestion for establishing the XRF approach to reveal the self-healing mechanism. The authors also thank Dr. Sonjong Hwang in Caltech for his assistance of conducting solid-state NMR tests.

Conflict of Interest

The authors declare no conflict of interest.

Data Availability Statement

The data that support the findings of this study are available from the corresponding author upon reasonable request.

Keywords

lithium dendrites, lithium metal battery, polymer electrolyte, solid-state electrolyte

Received: May 2, 2024
Revised: July 10, 2024
Published online:

[1] D. Lin, Y. Liu, Y. Cui, *Nat. Nanotechnol.* **2017**, *12*, 194.
[2] M. Papakyriakou, M. Lu, Y. Liu, Z. Liu, H. Chen, M. T. McDowell, S. Xia, *J. Power Sources* **2021**, *516*, 230672.
[3] C. Monroe, J. Newman, *J. Electrochem. Soc.* **2005**, *152*, A396.
[4] F. Han, A. S. Westover, J. Yue, X. Fan, F. Wang, M. Chi, D. N. Leonard, N. J. Dudney, H. Wang, C. Wang, *Nat. Energy* **2019**, *4*, 187.
[5] R. Raj, J. Wolfenstine, *J. Power Sources* **2017**, *343*, 119.
[6] C. L. Tsai, V. Roddatis, C. V. Chandran, Q. Ma, S. Uhlenbruck, M. Bram, P. Heitjans, O. Guillon, *ACS Appl. Mater. Interfaces* **2016**, *8*, 10617.
[7] V. Raj, V. Venturi, V. R. Kankanallu, B. Kuiri, V. Viswanathan, N. P. B. Aetukuri, *Nat. Mater.* **2022**, *21*, 1050.
[8] L. Porz, T. Swamy, B. W. Sheldon, D. Rettenwander, T. Frömling, H. L. Thaman, S. Berendts, R. Uecker, W. C. Carter, Y. M. Chiang, *Adv. Energy Mater.* **2017**, *7*, 1701003.
[9] H. Duan, Y. X. Yin, Y. Shi, P. F. Wang, X. D. Zhang, C. P. Yang, J. L. Shi, R. Wen, Y. G. Guo, L. J. Wan, *J. Am. Chem. Soc.* **2018**, *140*, 82.
[10] C. Yang, H. Xie, W. Ping, K. Fu, B. Liu, J. Rao, J. Dai, C. Wang, G. Pastel, L. Hu, *Adv. Mater.* **2019**, *31*, 1804815.
[11] T. Krauskopf, H. Hartmann, W. G. Zeier, J. Janek, *ACS Appl. Mater. Interfaces* **2019**, *11*, 14463.
[12] M. P. Scott, M. Rahman, C. S. Brazel, *Eur. Polym. J.* **2003**, *39*, 1947.
[13] H. Wang, H. Liu, Z. Cao, W. Li, X. Huang, Y. Zhu, F. Ling, H. Xu, Q. Wu, Y. Peng, B. Yang, R. Zhang, O. Kessler, G. Huang, J. Wu, *Proc. Natl. Acad. Sci. USA* **2020**, *117*, 11299.

[14] S. Wang, M. W. Urban, *Nat. Rev. Mater.* **2020**, *5*, 562.
[15] C. Jiang, Q. Jia, M. Tang, K. Fan, Y. Chen, M. Sun, S. Xu, Y. Wu, C. Zhang, J. Ma, C. Wang, W. Hu, *Angew. Chem., Int. Ed. Engl.* **2021**, *60*, 10871.
[16] a) H. Zhang, Z. Zeng, M. Liu, F. Ma, M. Qin, X. Wang, Y. Wu, S. Lei, S. Cheng, J. Xie, *Chem. Sci.* **2023**, *14*, 2745; b) H. Liang, Z. Ma, Y. Wang, F. Zhao, Z. Cao, L. Cavallo, Q. Li, J. Ming, *ACS Nano* **2023**, *17*, 18062; c) X. Liu, A. Mariani, T. Diemant, M. E. Di Pietro, X. Dong, A. Mele, S. Passerini, *Adv. Mater.* **2024**, *36*, 2309062; d) M. Huang, S. Feng, W. Zhang, J. Lopez, B. Qiao, R. Tatara, L. Giordano, Y. Shao-Horn, J. A. Johnson, *Chem. Mater.* **2019**, *31*, 7558.
[17] H. Xie, H. Liang, P. Kumar, H. Cheng, F. Zhao, Y. Wang, T. Cai, W. Wahyudi, Z. Ma, Q. Li, J. Ming, *Adv. Funct. Mater.* **2024**.
[18] Z. Cao, H. Liu, L. Jiang, *Mater. Horiz.* **2020**, *7*, 912.
[19] M. L. Jin, S. Park, J. S. Kim, S. H. Kwon, S. Zhang, M. S. Yoo, S. Jang, H. J. Koh, S. Y. Cho, S. Y. Kim, C. W. Ahn, K. Cho, S. G. Lee, D. H. Kim, H. T. Jung, *Adv. Mater.* **2018**, *30*, 1706851.
[20] X. Wang, C. Zhang, M. Sawczyk, J. Sun, Q. Yuan, F. Chen, T. C. Mendes, P. C. Howlett, C. Fu, Y. Wang, X. Tan, D. J. Searles, P. Kral, C. J. Hawker, A. K. Whittaker, M. Forsyth, *Nat. Mater.* **2022**, *21*, 1057.
[21] Y. Yang, S. Meng, E. G. Wang, *Phys. Rev. B* **2006**, *74*.
[22] Z. Cao, H. Liu, L. Jiang, *ACS Appl. Polym. Mater.* **2020**, *2*, 2359.
[23] R. J. Wojtecki, M. A. Meador, S. J. Rowan, *Nat. Mater.* **2011**, *10*, 14.
[24] F. Croce, G. B. Appetecchi, L. Persi, B. Scrosati, *Nature* **1998**, *394*, 456.
[25] B. B. Jing, C. M. Evans, *J. Am. Chem. Soc.* **2019**, *141*, 18932.
[26] M. Liu, S. Zhang, E. R. H. van Eck, C. Wang, S. Ganapathy, M. Wagemaker, *Nat. Nanotechnol.* **2022**, *17*, 959.
[27] a) G. Foran, N. Verdier, D. Lepage, C. Malveau, N. Dupre, M. Dolle, *Polymers* **2021**, *13*; b) M. Bakir, J. L. Meyer, A. Sutrisno, J. Economy, I. Jasiuk, *Sci. Rep.* **2018**, *8*, 14869.
[28] N. Wu, P. H. Chien, Y. Qian, Y. Li, H. Xu, N. S. Grundish, B. Xu, H. Jin, Y. Y. Hu, G. Yu, J. B. Goodenough, *Angew. Chem., Int. Ed. Engl.* **2020**, *59*, 4131.
[29] S. Luo, Z. Wang, X. Li, X. Liu, H. Wang, W. Ma, L. Zhang, L. Zhu, X. Zhang, *Nat. Commun.* **2021**, *12*, 6968.
[30] L. Wang, X. Sun, J. Ma, B. Chen, C. Li, J. Li, L. Chang, X. Yu, T. S. Chan, Z. Hu, M. Noked, G. Cui, *Adv. Energy Mater.* **2021**, *11*, 2100881.
[31] L. Zhang, M. Ling, J. Feng, L. Mai, G. Liu, J. Guo, *Energy Storage Mater.* **2018**, *11*, 24.
[32] a) D. Xu, J. L. Hawk, D. M. Loveless, S. L. Jeon, S. L. Craig, *Macromolecules* **2010**, *43*, 3556; b) G. Ianniruberto, G. Marrucci, *Macromolecules* **2015**, *48*, 5439.
[33] M. J. Webber, M. W. Tibbitt, *Nat. Rev. Mater.* **2022**, *7*, 541.
[34] a) K. Sui, X. Zhao, Z. Wu, Y. Xia, H. Liang, Y. Li, *Langmuir* **2012**, *28*, 153; b) D. Xu, S. L. Craig, *J. Phys. Chem. Lett.* **2010**, *1*, 1683.
[35] a) M. P. Goertz, X. Y. Zhu, J. E. Houston, *J. Polym. Sci., Part B: Polym. Phys.* **2009**, *47*, 1285; b) R. Weijermars, *Tectonophysics* **1986**, *124*, 325.
[36] K. Liu, A. Pei, H. R. Lee, B. Kong, N. Liu, D. Lin, Y. Liu, C. Liu, P. C. Hsu, Z. Bao, Y. Cui, *J. Am. Chem. Soc.* **2017**, *139*, 4815.
[37] a) S. Gürgen, M. C. Kuşhan, W. Li, *Prog. Polym. Sci.* **2017**, *75*, 48; b) E. Brown, H. M. Jaeger, *Rep. Prog. Phys.* **2014**, *77*, 046602.
[38] H. Gao, X. Ai, H. Wang, W. Li, P. Wei, Y. Cheng, S. Gui, H. Yang, Y. Yang, M. S. Wang, *Nat. Commun.* **2022**, *13*, 5050.
[39] Q. Zhao, S. Stalin, C.-Z. Zhao, L. A. Archer, *Nat. Rev. Mater.* **2020**, *5*, 229.
[40] H. Fan, C. Hartshorn, T. Buchheit, D. Tallant, R. Assink, R. Simpson, D. J. Kissel, D. J. Lacks, S. Torquato, C. J. Brinker, *Nat. Mater.* **2007**, *6*, 418.
[41] K. Liu, P. Bai, M. Z. Bazant, C.-A. Wang, J. Li, *J. Mater. Chem. A* **2017**, *5*, 4300.
[42] B. Xu, Z. Liu, J. Li, X. Huang, B. Qie, T. Gong, L. Tan, X. Yang, D. Paley, M. Dontigny, K. Zaghib, X. Liao, Q. Cheng, H. Zhai, X. Chen, L.-Q. Chen, C.-W. Nan, Y.-H. Lin, Y. Yang, *Nano Energy* **2020**, *67*, 104242.
[43] Z. Zeng, V. Murugesan, K. S. Han, X. Jiang, Y. Cao, L. Xiao, X. Ai, H. Yang, J.-G. Zhang, M. L. Sushko, J. Liu, *Nat. Energy* **2018**, *3*, 674.
[44] D. H. S. Tan, E. A. Wu, H. Nguyen, Z. Chen, M. A. T. Marple, J.-M. Doux, X. Wang, H. Yang, A. Banerjee, Y. S. Meng, *ACS Energy Lett.* **2019**, *4*, 2418.
[45] a) D. H. S. Tan, Y. T. Chen, H. Yang, W. Bao, B. Sreenarayanan, J. M. Doux, W. Li, B. Lu, S. Y. Ham, B. Sayahpour, J. Scharf, E. A. Wu, G. Deysher, H. E. Han, H. J. Hah, H. Jeong, J. B. Lee, Z. Chen, Y. S. Meng, *Science* **2021**, *373*, 1494; b) E. A. Wu, C. Jo, D. H. S. Tan, M. Zhang, J.-M. Doux, Y.-T. Chen, G. Deysher, Y. S. Meng, *J. Electrochem. Soc.* **2020**, 167.
[46] A. Shao, X. Tang, M. Zhang, M. Bai, Y. Ma, *Adv. Energy Sustainability Res.* **2022**, *3*.